Temporal and anteriorly positioned mitotic zones drive asymmetric microtubule patterns needed for Left-Right Organizer development.

Yan Wu[1,2,&], Yiling Lan[1,2,&], Favour Ononiwu[1,2,&], Abigail Poole[3], Kirsten Rasmussen[1], Jonah Da Silva[1], Abdalla Wael Shamil[1], Li-En Jao[4], and Heidi Hehnly[1,2,*]

[1]Department of Biology, Syracuse University, USA

[2]BioInspired Institute, Syracuse University, USA

[3]Worcester Polytechnic Institute, Worcester, MA

[4]Department of Cell Biology and Human Anatomy, University of California Davis School of Medicine, USA

[&] Equal contribution

*Lead contact, correspondence: hhehnly@syr.edu, Twitter: @LovelessRadio

Running Title: Zones of mitotic activity during LRO development

ABSTRACT

Cellular proliferation plays a crucial role in tissue development, including the development of the Left-Right Organizer (LRO), the transient organ essential for dictating the vertebrate LR body plan. Here we investigate cell redistribution mechanisms and the dominance of specific progenitor cells in LRO formation, addressing cell lineage and cell behavior questions. Using zebrafish as a model, we mapped all LRO (Kupffer's Vesicle, KV) mitotic events, revealing an FGF-dependent, anteriorly enriched mitotic pattern. Using a KV-specific fluorescent microtubule (MT) line, we found that mitotic events align their spindle along the KV's longest axis until the rosette developmental stage, where "spinning" spindles followed by exclusion from KV occur. Daughter cells that remain are linked by cytokinetic bridges, shaping anteriorly focused MT patterns that precede apical actin recruitment. Our findings underscore the importance of spatially regulated mitotic events in establishing MT and actin pattern formation essential for LRO development.

Introduction

The Left-Right Organizer (LRO) is one of the earliest ciliated organs formed during vertebrate development. It is a small and yet important structure—e.g., the node in mice and Kupffer's vesicle (KV) in zebrafish—that only exists transiently during early embryogenesis to help establish the left-right patterning of the body plan. The LRO initiates the development of the left-right asymmetry through its cilia-driven, directional fluid flow that induces asymmetric gene expression (summarized in [1–4]). Compromised formation of LRO or its ciliary motility (e.g., mutations in the axonemal dynein motor [5–7]) would lead to LR patterning defects.

Previous studies using the mouse and zebrafish models (**Fig. 1A**, reviewed for fish in [1,3], recent study in mice [8]) have shown that LRO is formed through the organization of the LRO progenitor cells (e.g., dorsal forerunner cells in zebrafish) into rosette-like structures before displaying epithelial-like characteristics and initiating lumen formation. Using in vitro three-dimensional (3D) cultured Madine-Darby Canine Kidney (MDCK) cells suspended in extracellular matrix [9–12], lumen formation has been further shown to be preceded by cell division, followed by the establishment of apical polarity and cell-cell contacts adjacent to the cytokinetic bridge. However, those in vitro 3D cell culture models do not recapitulate the mesenchymal to epithelial transition, nor the dynamic changes in cell shape and expression profiles during LRO formation in a living organism. In addition, without the in vivo biological context, different in vitro 3D models often lead to different conclusions. For example, the MDCK [13] and Inner Medullary Collecting Duct (IMCD)[14] models showed a different timing of cilia formation during LRO formation. Therefore, despite the insights gained from different in vitro 3D cell culture models, the cellular mechanisms and signals underlying the formation and maintenance of the LRO remain unresolved.

To understand how a functional LRO is formed in a living organism—from a small group of precursor cells to a fluid-filled sac lined with both motile and non-motile ciliated cells [15,16], we studied the development of the Kupffer's Vesicle (KV), the zebrafish LRO, at single-cell resolution using a series of novel transgenic zebrafish

lines and cell biological techniques, including high-resolution live microscopy, lineage tracing, laser ablation, and pharmacological treatments. Our study shows that FGF signaling-mediated early divisions of KV precursor cells are pivotal for proper KV development as the progeny of these early division events constitute a proportion of cells in the mature KV. Our data also suggest that apical microtubule bundles—originated from the daughter cells of the early KV precursors—may facilitate actin recruitment that is crucial for KV development.

Results

Identification of an anteriorly positioned and pre-lumen enriched KV mitotic events and their post-mitotic distribution map. To follow how the KV is formed at single-cell resolution in a living vertebrate, we generated a double transgenic zebrafish line Tg(Sox17:GFP-CAAX; h2afx:h2afv-mCherry), where the KV progenitor cells, i.e., the dorsal forerunner cells (DFCs), were labeled by membrane-bound GFP while all DNA was labeled by the red fluorescent protein mCherry. We followed the movement and division of DFCs by time-lapse microscopy starting at approximately 8 hours post fertilization (hpf) when 15–30 DFCs have formed (**Fig. 1A, 1B, Video S1**). The KV transitions from approximately 15 DFCs that then expand in number and organize into rosette configurations before transitioning to a lumen (**Fig. 1A**). Mitotic events predominantly occurred in the anterior region of the future KV before lumen opening (83.3% of all mitotic cells for a representative embryo in **Fig. 1B, S1A-B, Video S1**) and was confirmed across multiple embryos (**Fig. 1C**). The same conclusion was also reached when fixed Sox17:GFP-CAAX embryos were analyzed by anti-phospho-histone 3 (PH3) (a mitotic cell marker) staining at 8 hpf, where we detected a significant fraction of mitotic events in the anterior zone (**Fig. 1D, 1E**) with an enrichment to the left anterior quadrant (**Fig. S1C**).

Next, we investigated the distribution of post-mitotic daughter cells from KV precursors in the fully formed KV. For this purpose, embryos were incubated with BrdU

from 70% epiboly to 12 hpf to label cells that had undergone cell division before KV completion at 12 hpf. We observed that these BrdU-positive (post-mitotic) cells were distributed throughout the KV, with a significantly higher concentration in the posterior region (**Fig. 1D-E, Fig. S1D**).

To determine specifically how KV progenitor cells and their progeny reposition following cell division, we performed cell lineage tracing analysis of H2B-Dendra expressing, Sox17:GFP marked KV precursor cells (**Fig. 1F-G**). In this experiment, individual H2B-Dendra-positive cells (green) were photoconverted at metaphase and the trajectories of the resulting daughter cells (red) were followed throughout the KV developmental stages until lumen expansion (**Fig. 1A, Fig. 1F-G**). We found that the daughter cells of a given KV precursor stay together and move within the KV boundary after division (representative events shown in **Fig. 1F'** and **Fig. S1E**). Among 8 photoconverted metaphase cells and their progeny we followed, all the daughter cells did not divide again during KV development, indicating that at least 50% of KV progenitor cells divide once and only once after 8 hpf (**Fig. 1H**). We found that most of the post-mitotic cells were organized in the anterior region of the KV until the rosette stage at the 120 min time point, and then redistributed to the posterior region of the KV during lumen formation (180 min, **Fig. 1H, 1I**). When we determined the ratio of anteriorly versus posteriorly positioned post-mitotic cells, this ratio started to approach 1 right before lumen opening and after the cell number in the KV had reached its maximum (**Fig. 1I**). Together these results indicate that KV progenitor cells divide preferentially in the anterior region of the future KV, and the resulting post-mitotic cells were incorporated throughout the mature KV, with more cells in the posterior than in the anterior regions.

An anterior/posterior FGF signaling gradient is required for anterior zones of mitotic activity. Since the early mitotic events of KV precursors took place predominantly anterior to the location of the future KV (**Fig. 1**), we hypothesized that an anteroposterior signal(s) coordinates the cell division and the later LRO

development. To test this, we individually inhibited the major signaling pathways that had been implicated in LRO development [17–19] using well-established pharmacological inhibitors, and then determined whether KV development is affected (**Fig. 2A, Fig. S2A-E**). We found that blocking fibroblast growth factor (FGF) signaling, but not Wnt or Shh signaling, attenuated the division of KV precursors through PH3 staining at 8 hpf (**Fig. 2B, 2D**) and caused KV cells to not expand in number at pre-lumenal to luminal stages (**Fig. S2E**). Inhibiting FGF signaling also disrupted spatially concentrated mitotic events in the anterior quadrant of the developing KV and caused severe KV developmental defects (**Fig. 2B, 2E-F, S2A-D**). Similar to FGF inhibition causing a complete loss of the anterior-enriched mitotic zone (median of 0.5 of anteriorly to posteriorly positioned events), compared to control and Wnt inhibition conditions where most events were enriched to the anterior region (median of 1.0 and 0.835 respectively), and significant decrease in mitotic index (**Fig. 2D** and **2E**), only FGF inhibition demonstrated a significant defect in KV development measured by lumen area (**Fig. 2B, 2F, S2A-C**). These findings suggest that an anteroposterior FGF signaling gradient is required for the mitotic activity in the anterior region of the developing KV.

To determine whether loss of the anteriorly biased mitotic events is sufficient to disrupt proper KV formation at the later stage, we disrupted mitotic events independent of FGF signaling using pericentrin maternal-zygotic mutant embryos (*pcnt*$^{-/-}$, [20]) and assessed KV development. Pericentrin is a centrosomal protein known to regulate spindle assembly, and loss of pericentrin can result in a decrease in mitotic entry and failure to complete mitosis [21–25]. We found that the overall cell division (**Fig. 2C-D**) and the anterior enrichment of mitotic events (**Fig. 2E**) of KV precursors decreased significantly in maternal-zygotic *pcnt*$^{-/-}$ embryos. Associated with this decrease in anteriorly positioned mitotic events was also the disruption in KV development, demonstrated by a significant reduction in the lumen area at 12 hpf (**Fig. 2C, 2F**). Together, these findings suggest that a potential anteroposterior FGF signaling regulates the early, anteriorly biased KV precursor divisions, which are required for

subsequent KV formation.

Early KV mitotic events hold greater significance to KV development compared to later KV mitotic events. To determine the role and relevance of individual KV mitotic events, we employed laser ablation to selectively remove mitotic events (**Fig 3A-B, Video S2**). Temporal characterization of mitotic events involved six ablation conditions, encompassing two control scenarios—no ablation and ablation of non-mitotic cells (3 to 8 cells). The first experimental ablation comparison was with ablating all mitotic events compared to no ablation controls (**Fig. 3C, 3E, 3G**). Then specific temporal ablation patterns were performed and compared (**Fig. 3D, 3F, 3H**): (1) ablating the first 4 mitotic events when fewer than 20 KV precursor cells were present (Condition 1); (2) ablating 4 mitotic events when more than 20 KV precursor cells were present (Condition 2); and (3) ablating all mitotic events when more than 20 KV precursor cells were present (Condition 3). During video acquisition, mitotic cells were ablated by positioning a region of interest (ROI) over the metaphase plate, distinguished by h2afv-mCherry, and delivering a 355 nm pulsed laser within the ROI (**Fig 3B, Video S2**). Monitoring encompassed all cells, including the cell with the ablated plate, and revealed no evident apoptotic events in the non-ablated cells. The ablated cells failed to complete mitosis and were ultimately extruded from the developing KV.

Our studies indicate that the first 4 KV divisions are crucial for KV development, while later divisions near lumen formation are not essential (**Fig 3C-I**). KVs did not significantly increase in cell number between 8 hpf and 12 hpf when all mitotic events were ablated or when all mitotic events were ablated with more than 20 KV precursor cells present (**Fig 3E-F**), suggesting the importance of mitotic events in KV cell number expansion during development. Significant defects in lumen formation kinetics (**Fig 3C-D, 3G-H, Video S3**) and the final lumen area (**Fig 3I**) occurred when all mitotic events or only the first 4 events were ablated (Condition 1), but not when later mitotic events were ablated (Condition 2 and 3), compared to non-mitotic cell ablation control (**Fig 3I**). Embryos subjected to ablation and monitoring for lumen formation kinetics

(**Fig 3C-D**) were fixed at 12 hpf and immunostained for cilia. Like lumen formation defects, significant reductions in the percentage of ciliated cells were observed only when ablating all mitotic events or the first 4 events (**Fig 3C-D, 3J**). These findings underscore the pivotal role of early KV mitotic events in orchestrating both KV development and overall KV ciliogenesis.

KV spindles stably align along KVs longest axis until the KV starts rounding, then spindles spin and are extruded. Proper spindle orientation during mitosis is important for tissue morphogenesis [26,27]. Given the significance of early mitotic events in KV development (**Fig. 3**), we aimed to understand the relationship between spindle positioning and division timing by analyzing the spindle behaviors in the KV precursor cells over time. To specifically label microtubules (MTs) in KV precursors, we adapted a similar strategy we have used before [28] to generate a Tg(Sox17:EMTB-3xGFP) transgenic line, where the MTs in KV precursors were labeled by GFP-tagged MT-binding protein ensconsin. This transgenic line allowed us to discern changes in intracellular MT patterning during KV development in live embryos for the first time (**Fig. 4A**). Through a series of time-lapse imaging analysis, we found that the spindles of the dividing KV precursors formed and positioned primarily along the long axis of the developing KV in the pre-lumenal stage (**Fig. 4A**, 8 min, **Video S4**). As the KV precursors were incorporated to form the rosette structure, the MT bundles started to concentrate at the cytokinetic bridge near the rosette center (**Fig 4A**, 97 min, **Video S4**). Strikingly, as the KV structure went from a structure that had a long and short axis (**Fig 4A**, 8 min) to a structure that was more rounded (**Fig 4A**, 97 to 163 min) the spindles that formed rotated dramatically, that we refer to as “spinning spindles”, and were subsequently extruded from the KV (**Fig 4A**, 163 min, **Fig 4B**, **Video S4**). These findings indicate that the rosette was formed by the daughter cells of the early-dividing KV precursors. In contrast, daughter cells from the later cell divisions were excluded from the KV. These results also explain why the later, but not the early, division events are dispensable for KV formation in our ablation studies (**Fig. 3**). To our knowledge,

this is also the first evidence to show that cell extrusion is part of the developmental program of KV formation, akin to the cell extrusion process that has been documented in other developmental contexts such as the generation and maintenance of the tight epithelial barrier [29].

To characterize the robustness of these observed events, the aspect ratio, defined as the longest axis over the shortest axis of the KV (**Fig 4C**), was measured during KV development (**Fig 4D**) and compared to the degree of spindle angle changes per minute (**Fig 4E**). Time was normalized to lumen opening so that negative time values are pre-lumen formation and positive values are post lumen formation (**Fig 4D- 4F**). We identified that as the aspect ratio of the KV approached a mean value of less than 2 (dashed line, **Fig 4D**), that spindles started to spin which relates to an increased angle change (degree/min or spindle rotation rate, **Fig 4E,** direct comparison between A.R. less than 2 and greater than 2 in **4E'**). A population of these mitotic events then become extruded once the lumen starts to open (**Fig 4F,** direct comparison between A.R. less than 2 and greater than 2 in **4F'**). When we ablated the first four mitotic events (condition 1) or ablated all mitotic events post-reaching 20 KV progenitor (condition 3, refer to **Fig. 3A, 4G, Video S5**), we observed a loss of post-mitotic extrusion events. Interestingly, even when we only ablated the first 4 mitotic events, no later extrusion events occurred, suggesting that extrusion may be a response to cell packing. This suggests that if early events are alleviated, later division events can still be incorporated into the KV, but the KV doesn't develop appropriately (**Fig. 3**).

Anterior division events lead to anterior focused cytokinetic bridge remnant MT bundles at the rosette which precede actin recruitment. During the early stages of KV development when there are approximately 20 KV precursor cells, the daughter cells of those early precursors have consistently been incorporated into the developing KV structure (**Fig. 4**) with the cytokinetic bridges of those daughter cells aligning towards the emerging rosette structure (**Fig. 5A-B**). During this period, we found that filamentous actin (visualized by lifeact-mRuby) was recruited to these bridge sites

shortly after the enrichment of the apical MT bundles (**Fig. 5B-C, Video S6**). While the actin accumulation in the rosette has been observed before [8,30], this concurrent enrichment of MT and actin bundles at the rosette center has not been reported. This observation suggests a potential coordination between MT and actin dynamics during KV development. This observation is also different from the findings in mammalian cell culture systems, where the MTs at the cytokinetic bridge usually disassemble prior to abscission [31,32]. Here in the developing KV of the live zebrafish embryo, little to no MTs were disassembled after abscission (indicated by the loss of the mKate-MKLP1-positive midbody, used in [33], compare 0m to 2m, yellow arrow marks loss, **Fig. 5D**). The MT bundles at the rosette center even persist several minutes after abscission (2m-8m in **Fig. 5D**).

To test the role of early KV mitotic division events on the potential interplay between the apical MT and actin enrichment at the rosette center further, we performed laser ablation experiments targeting the initial 4 divisions of the KV precursors described earlier (Condition 1, **Fig. 3**). We found that upon the loss of the 4 early mitotic events, both apical MT and actin enrichments at the rosette center were reduced, especially in the anterior region (**Fig. 5E–H**). Together with the observation that the enrichment of the apical MT bundles preceded that of the filamentous actin (**Fig. 5B**), these results suggest that the apical MT bundles derived from cytokinetic bridges originated from the daughter cells of the early KV precursors may facilitate actin recruitment, which is crucial for actomyosin contractility events during rosette to lumen transition [34].

Discussion

Recent studies of LRO formation have elucidated the fundamental role of LRO progenitors in forming the rosette-like structure with epithelial-like characteristics before the initiation of lumen formation [8,15,30]. However, the steps preceding lumen formation is not clear, especially in the context of a living embryo. By studying KV formation in zebrafish embryos with novel transgenic and cell biological tools, our

results suggest a model in which FGF-mediated signals induce the proliferation of a subset of early KV precursor cells, predominantly located anteriorly to the developing KV. Their progeny are then incorporated into the rosette before lumen formation, whereas the progeny from the later cell divisions were excluded (**Fig. 5l**). How FGF signaling coordinates the proliferation of the early KV precursors is an important question that awaits future studies.

Our data also show that the apical MT bundles originated from the daughter cells of the early KV precursors persist after cytokinesis. These apical MT bundles may facilitate actin recruitment, which is crucial for the formation of the apical membrane during KV formation. Interestingly, in filamentous fungi, fission yeast, and the moss *Physcomitrella patens*, polarity markers are delivered on MTs toward the cell extremes, subsequently promoting actin polymerization in a possibly analogous manner to what we are observing here [35–37].

Centrosome positive and negative microtubule organizing centers (MTOCs) can rely on actin organization for their positioning and function[38–40] and in some cases MTOCs have been identified to organize actin [41]. While the centrosome with its associated centrioles traditionally functions as the primary MTOC in most animal cells to organize MTs, our results suggest that KV cells maintain cytokinetic bridge MTs for an alternative structure used during epithelialization. MT-bundled structures that aren't assembled by a bonafied centrosome have been reported at the base cof C. elegans sensory cilia [42] and in the early mouse embryo [43]. In the KV, one potential possibility for these bundled MTs is that they are potentially used to help reposition the centrosome and intracellular forming cilia to the apical membrane that occurs during this time [15,44]. As KV cells progress from a mesenchymal to epithelial-like state, the centrosome transforms into a basal body responsible for cilium assembly in a subset of KV progenitor cells before rosette formation [15]. The centrosome has been documented to decrease its MTOC function when required to reposition where it can transport along pre-existing MTs to get to its future site of function[45,46]. Thus, KV cells

may need to maintain an additional MT based structure, cytokinetic bridge derived MTs, to assist in a mesenchymal to epithelial transition (**Fig. 5l**).

Figure Legends

Figure 1. *Identification of an anteriorly positioned and pre-lumen enriched Kupffer's Vesicle (KV) mitotic events and their post-mitotic distribution map.*

(A) Model depicting KV cells transitioning from a small population, likely proliferative, then organize into rosette structures then transition to a cyst of ciliated (light blue) cells surrounding a fluid filled lumen.

(B) Representative confocal volumetric projections from live KV development video (refer to **Video S1**). Pre-KV lumen time point (-22 min before lumen opening) and post-lumen (26 min past lumen opening) shown. KV cell membranes marked by Sox17:GFP-CAAX (magenta) and nuclei with h2afx:h2afv-mCherry (cyan-non-mitotic, yellow-mitotic). Scale bar, 10 μm.

(C) Percentage of KV cells that are mitotic across a 120 min video time course (n=3 embryos ±SEM).

(D) Confocal projections of mitotic (Phospho-Histone H3, PH3, magenta) and post-mitotic (BrdU, magenta) events at pre lumen (8 hpf) and post lumen (12 hpf). KV cell membranes marked with Sox17:GFP-CAAX (inverted gray). Scale bar, 10 μm.

(E) Percentage of PH3 and BrdU-positive cells in the anterior vs posterior regions of the KV (n=4 clutches, 36 embryos; and n=3 clutches, n=17 embryos respectively). Each point represents an embryo, the point colors represent clutch, n=3 clutches, $^{**}p<0.01$.

(F-G) Confocal projections of H2B-Dendra photoconversion (non-photoconverted black nuclei, photo-converted in fire-LUT). Cyan and magenta outlines mark mitotic photoconverted event at 10 min. A total of 8 mitotic events were photoconverted. Daughter cell positioning at (**F**) 96 min and (**G**) 180 min shown. **(F')** Trajectory of marked mitotic events from division completion to 96 min. KV cell boundary, green outline. Scale bar, 10 μm.

(H) Temporal schematic of KV mitotic event for representative embryo in (**F**), daughter cells did not divide again.

(I) KV cell number (blue) and ratio of post mitotic anterior positioned or posterior positioned cells were calculated over time from acquisition in (**F-G**).
Statistical results detailed in **Table S1**.

Figure S1. *Identification of an anteriorly positioned and pre-lumen enriched Kupffer's Vesicle (KV) mitotic events and their post-mitotic distribution map.*
(A) KV mitotic cell position was mapped during KV development from **Video S1**. Different colors indicate different 20 min time bins pre and post lumen formation.
(B) Time bins from (**A**) and **Video S1** were mapped as percentage of mitotic KV cells in relation to lumen formation.
(C, D) Bubble plot depicting the positioning of mitotic event (PH3, **C**) and post mitotic cells (BrdU-positive, **D**) in KV at 8 and 12 hpf respectively. Large circle, represents > 7 events. Small circle represents 3 events. Tiny circle represents 1 event. n=26 embryos, across 3 clutches.
(E) 2 mitotic photoconversion events shown in **Fig 1F** highlighted. Scale bar, 10 μm.
Statistical results detailed in **Table S1**.

Video S1. *Identification of an anteriorly positioned and pre-lumen enriched Kupffer's Vesicle (KV) mitotic events and their post-mitotic distribution map.* Live confocal registered video showing mitotic events within KV in an embryo from the outcross of Sox17:GFP-CAAX and H2afx:h2afv-mCherry transgenic lines. KV cell plasma membranes marked by magenta (Sox17: GFP-CAAX) and nuclei (cyan, H2afx: h2afv-mCherry). Scale bar, 20 μm. Refer to **Fig 1B**.

Figure 2. *An anterior/posterior FGF signaling gradient is required for anterior zones of mitotic activity.*
(A) Model illustrating experimental approach to identify whether a signal influenced mitotic events and how those events contribute to KV development.
(B-C) Confocal projections of pre-lumen (8hpf, top) and post-lumen (12 hpf, bottom)

KVs treated with DMSO, 10 μM XAV939 (Wnt inhibitor), and 1μM infigratinib (FGF inhibitor) (**B**) or lacking Pericentrin (*pcnt*$^{-/-}$) compared with wild-type control (*pcnt*$^{+/+}$) (**C**). KV cell membranes marked with Sox17:GFP-CAAX (inverted gray), mitotic events with PH3 (magenta). Lumens highlighted in gold. Scale bar, 10 μm.

(D-F) Percent of mitotic KV cells (**D**), anterior vs poterior positioned mitotic events (**E**), and lumen area (**F**) were measured for n>33 embryos (small dots represent embryos, **D-F**) across n≥3 clutches (large dots represent clutch, **D, F**) per condition. Graphs are scatter plots with mean of clutches shown ±SEM (**D,F**) or a violin plot (**E**). DMSO, 10 μM XAV939, 1 μM infigratinib, pcnt$^{+/+}$ and pcnt$^{-/-}$ shown. *p<0.05, **p<0.01, ***p<0.005, ****p<0.0001, n.s. not significant. Statistical results detailed in Table S1.

Figure S2. *An anterior/posterior FGF signaling gradient is required for anterior zones of mitotic activity.*

(A-C) Confocal projections of post lumen (12 hpf) embryos treated with methanol, 50 μM Cyclopamine (**A**), DMSO, 10 μM XAV939 (**B**), and 0.5μM, 1μM, 3μM, 5μM infigratinib (**C**). KV cell membranes marked with Sox17:GFP-CAAX (inverted gray), lumens highlighted in gold. Scale bar, 10 μm.

(D) KV morphologies characterized following infigratinib treatment with varying concentrations at 12 hpf, n>25 embryos per condition across 2 clutches.

(E) KV cell number at pre-lumen (8hpf) and post-lumen (12 hpf) following DMSO, 10 μM XAV939, and 1 μM infigratinib treatment. KV cell number was compared between *pcnt*$^{+/+}$ and *pcnt*$^{-/-}$ zebrafish. n>16 embryos (small dots represent embryos) across n≥3 clutches (large dots represent clutch) per condition. Graphs are scatter plots with mean of clutches ±SEM shown, n≥3 clutches. **p<0.01, ***p<0.005, ****p<0.0001, n.s. not significant. Statistical results detailed in **Table S1.**

Figure 3. *Early KV mitotic events hold greater significance to KV development compared to later KV mitotic events.*

(A) Model illustrating laser ablation conditions during KV development.

(B) Representative images of KV ablation experiment showing a pre-ablation and post-ablation cell. White arrow is KV cell ablated. KV cell membranes marked by Sox17:GFP-CAAX (magenta) and nuclei with h2afx:h2afv-mCherry (cyan). Scale bar, 10 μm. Refer to **Video S2**.

(C, D) Confocal projections taken from a video acquisition (0-200m, left, Sox17:GFP-CAAX, inverted gray; lumen, gold, Refer to **Video S3**). The embryo was then fixed at 6SS (12 hpf) and stained for cilia (acetylated tubulin, cyan, right; Sox17:GFP-CAAX in magenta). Number of cilia in each representative image labeled. Scale bar, 10 μm.

(E, F) Truncated violin plot depicting the number of KV cells at 8 hpf and 12 hpf for no ablation and ablating all mitotics (**E**) or ablation conditions 1, 2, or 3 (**F**) across n≥3 embryos (each point represents a single embryo). Median denoted with black line and early/late temporal zone threshold (20 cells) denoted with grey dashed line.

(**G, H**) Lumen area was measured over time for over 100 min for no ablation (control) and ablating all mitotics (**G**) or ablation conditions 1, 2 or 3 (**H**). n≥3 ±SEM embryos measured per condition. Unpaired two-tailed t-tests in (**G**), One way ANOVA with Dunnett's multiple comparison in (**H**). *p<0.05, **p<0.01, ***p<0.005, n.s. not significant.

(**I, J**) Truncated violin plots depicting KV lumen area (12 hpf, **I**) and percentage of ciliated KV cells (**J**). n≥3 embryos at each condition. One way ANOVA with Dunnett's multiple comparison to non-mitotic ablation controls. *p<0.05, ***p<0.005, n.s. not significant.

Statistical results detailed in **Table S1**.

Video S2. *Early KV mitotic events hold greater significance to KV development compared to later KV mitotic events.*

Live confocal video showing ablated cells failing to complete mitosis within KV in a Sox17:GFP-CAAX, H2afx:h2afv-mCherry embryo. Sox17:GFP-CAAX (magenta) and H2afx:h2afv-mCherry (cyan) shown. Scale bar, 10 μm. Refer to **Fig 3B**.

Video S3. *Early KV mitotic events hold greater significance to KV development compared to later KV mitotic events.*

Live confocal video showing lumen formation from a Sox17:GFP-CAAX, H2afx:h2afv-mCherry embryos under different laser ablation conditions. Sox17:GFP-CAAX (inverted gray) shown. Scale bar, 10 μm. Refer to **Fig 3C, D**.

Figure 4. *KV spindles stably align along KVs longest axis until the KV starts rounding, then spindles spin and are extruded.*

(**A, B**) Time-lapse video of microtubule organization during KV formation (Sox17: EMTB-3xGFP, gray). KV are outlined (white dashed line). Highlighted are spindles (yellow arrows) and cytokinetic bridges (pink arrows). The blue boxed region is magnified in (**B**) showcasing a spinning mitotic spindle that becomes extruded. Mitotic spindle poles noted with blue and pink arrowheads. Extruded cytokinetic KV cell post spinning event outlined (orange dashed line). Scale bars, 10 μm. Refer to **Video S4**.

(**C**) Methods to measure KV aspect ratio (A.R.) and the rate at which a spindle rotation rotates ($\Delta\angle a$) illustrated in model.

(**D, E**) Floating bar graph depicting the maximum, minimum and mean of KV A.R. (**D**) and mean spindle rotation rates (**E**) over 20 min binned time periods relative to lumen formation. The gray dashed line marks when A.R. equals 2. n=7 embryos measured across 6 clutches.

(**E'**) Spindle rotation rates were compared when A.R. was <2 or >2 from data sets in (**E**). 32 spindle poles from n=7 embryos across 6 clutches were monitored. Unpaired two-tailed t-tests, **p<0.01.

(**F**) Floating bar graph depicting the maximum, minimum and mean of the percentage of mitotic events with post mitotic cell extruded at various time bin (each 40 min) relative to lumen formation. n=7 embryos from 6 clutches. (**F**') Percentage of mitotic events with post mitotic cell extruded pre- versus post-lumen formation. n=7 embryos from 6 clutches. Unpaired two-tailed t-tests, *p<0.05,

(**G**) Truncated violin plot depicting the frequency of mitotic events with post mitotic cell

extruded in no ablation controls or mitotic ablated condition 1 and 3. n>6 embryos measured over 6 clutches. Unpaired two-tailed t-tests, *p<0.05. Refer to **Video S5**. Statistical results detailed in **Table S1**.

Video S4. *KV spindles stably align along KVs longest axis until the KV starts rounding, then spindles spin and are extruded.*

Live confocal video showing microtubules (grey, Sox17:EMTB-3xGFP) in KV (left). Highlighted from KV video on left is a spinning spindle (middle) and cell extrusion event (right). Scale bar, 20µm. Refer to **Fig 4A, B.**

Video S5: *KV spindles stably align along KVs longest axis until the KV starts rounding, then spindles spin and are extruded.*

Time lapse data set of Sox17:EMTB-3xGFP (MTs, Fire LUT) embryos under control (no ablation) conditions compared to laser ablation conditions (cond.1, first four mitotic events ablated; and cond. 3, all mitotic events ablated after KV reaches 20 cells). Scale bar: 20µm. Refer to **Fig 4G**.

Figure 5: *Anterior division events lead to anterior focused cytokinetic bridge remnant MT bundles at the rosette which precede actin recruitment.*

(A-B) Time-lapse video of actin organization (lifeact-mRuby, magenta in **A** and FireLUT in **B**) and microtubule (EMTB-3xGFP, inverted grey) rearrangement during KV formation. The region denoted by the magenta dashed line in (**A**) is shown in (**B**). Scale bar, 10 µm. Refer to **Video S6**.

(C) Actin intensity (lifeact-mRuby) was measured over 15 minutes for n=3±SEM newly formed cytokinetic bridges (marked by EMTB-3xGFP) from representative embryo.

(D) Time-lapse video of an abscission event (yellow arrow) with a cytokinetic bridge and midbody labeled with mKate-MKLP1 (cyan) and microtubules (EMTB-3xGFP, magenta). Insets show MKLP1 (cyan) decorating a midbody (0 min), bridge abscission (yellow arrow, 2 min), and midbody loss at 8 min. Scale bar, 10 µm.

(E) Confocal projections were captured from live video acquisitions of embryos under two conditions: no ablation control and ablated mitotic condition 1 (EMTB-3xGFP microtubules, Fire-LUT). The anterior and posterior regions of the KV are demarcated by a white dashed line. Scale bar, 10 μm.

(F) Truncated violin plot depicting the ratio of microtubules fluorescence intensity at anterior of lumen over posterior at the rosette to lumen transition. Unpaired two-tailed t-tests, n≥3, *p<0.05.

(G) Confocal projections of KV (left) and magnified early lumen (highlighted by orange box and magnified 2X on right, actin in Fire-LUT) depicting actin (magenta) and microtubules (Sox17:EMTB-3xGFP, inverted gray). Scale bar, 10 μm.

(H) Truncated violin plot depicting the ratio of actin fluorescence intensity at anterior over posterior domains with a KV transitioning from rosette to lumen. Unpaired two-tailed t-tests, n≥3, **p<0.01.

(I) Model for how KV cells incorporate mitotic and post-mitotic events into a developing KV.

Statistical results detailed in **Table S1**.

Video S6: *Anterior division events lead to anterior focused cytokinetic bridge remnant MT bundles at the rosette which precede actin recruitment.* Time lapse max-projected dataset of actin (lifeact-mRuby, magenta) during KV lumen formation and KV microtubules (Sox17:EMTB-3xGFP, shown in inverted gray). Scale bar, 20 μm. Refer to **Fig 5A-5B**.

Acknowledgements

We thank SU's BioImaging Core for their assistance and In Vivo Biosystems for helping us create the Sox17:EMTB-3xGFP line. This work was supported by National Institutes of Health Grants no. R01GM-127621 (H.H.) and no. R01GM-130874 (H.H.).

EXPERIMENTAL PROCEDURES

Resource Availability

Lead contact: For further information or to request resources/reagents, contact Lead Contact, Dr. Heidi Hehnly (hhehnly@syr.edu)

Materials availability: New materials generated for this study are available for distribution.

Data and code availability: All data sets analyzed for this study are displayed.

Experimental model and subject details

Fish Lines

Zebrafish lines were maintained in accordance with protocols approved by the Institutional Animal Care Committee of Syracuse University (IACUC Protocol #18-006). Embryos were raised at 28.5°C and staged (as described in [47]). Wildtype and/or transgenic zebrafish lines used for live imaging and immunohistochemistry are listed in Key Resource Table.

Method Details

Chemical inhibitors

Dechorinated live embryos were treated with 10 μM XAV939 (Sigma-Aldrich), 0.5 to 5 μM Infigratinib (MedChem Express), and 50 μM cyclopamine (Sigma-Aldrich) were prepared. Tg(sox17:GFP-CAAX) transgenic zebrafish embryos were dechorionated on 2% agarose pad dishes and at 50% epiboly incubated with vehicle control (0.4%

DMSO, 0.5 % Methanol) and in listed concentrations of inhibitor diluted in zebrafish embryo water (0.03% sea salt, $1*10^{-5}$% Methylene Blue, RO water) and also taking into account the volume of agarose pad. Embryos were incubated to 8 hours post fertilization (hpf) and 12 hpf and fixed in 4% paraformaldehyde (PFA) (refer to immunofluorescence section).

BrdU Incorporation

Tg(sox17:GFP-CAAX) embryos were dechorionated at 50% epiboly, followed by incubation in E3 buffer (5mM NaCl,0.17mM KCl, 0.33mM $CaCl_2$,0.33mM $MgSO_4$) for 15 minutes at room temperature. Embryos were then incubated in 10 mM BrdU in E3 buffer containing 12% DMSO and maintained at temperatures between 28.5 and 30°C until 10 hpf. Following serial dilution washes in E3 medium, the embryos were incubated until 12 hpf and fixed in 4% PFA and overnight dehydration in cold methanol at -20°C. Embryos then underwent a sequential rehydration process using methanol to PBST mixture ratios of 3:1, 1:1, and 1:3 for 5 minutes each step. Embryos were refixed for 15 minutes in 4% PFA with 0.5% Triton-X 100, followed by acid treatment with 2N HCl for 1 hour and subsequent neutralization in 0.1M borate buffer (0.1M Boric Acid, 0.076M NaOH) for 20 minutes. Then standard immunofluorescent approaches were used to label for BrdU (anti-BrdU, mouse, 1:100, Sigma-Aldrich,11170376001: BMC9318). See immunofluorescence section and Key Resource Table.

Plasmids and mRNA for injection experiments

Plasmids were generated using Gibson cloning methods (NEBuilder HiFi DNA assembly Cloning Kit) and maxi-prepped before injection and/or transfection. mRNA was made using mMESSAGE mMACHINE™SP6 transcription kit. See key resource table for a list of plasmid constructs and mRNA used. Injections of 1 cell staged embryos were performed as described in [48].

Immunofluorescence

Immunostaining for phospho-histone H3 (PH3), acetylated tubulin and GFP, Tg(sox17:GFP-CAAX) transgenic zebrafish embryos were fixed at 8 and 12 hours post fertilization (hpf) using 4% PFA with 0.5% Triton X-100 overnight at 4°C. Embryos were dechorinated after washing with PBST (0.1% Tween-20 in Phosphate Buffered Saline (PBS)) 3 times. Embryos were blocked in wash solution (1%DMSO,1% BSA,0.1%Triton-X) for 1 hour at room temperature with gentile agitation. Primary antibody incubation (diluted in wash solution) occurs overnight at 4°C. Primary antibodies used include: anti-Phospho-Histone H3 (Rabbit) antibody (1:200, Cell Signaling Technology, 9701S), Anti-GFP (Chicken) (1:300, GeneTex, GTX13970: AB_371416) or Anti-Acetylated Tubulin (Mouse) (1:300, Sigma Aldrich,T6793: RRID: AB_477585), Anti-GFP (Rabbit) (1:300, Molecular Probes, A-11122: AB_221569), refer to Key Resource Table. Embryos were then washed and incubated with secondary antibodies for 2-4 hours at room temperatures or overnight at 4°C. Secondary antibodies used include: Alexa Fluor Anti-Mouse 568 (1:300, Life Technologies, A10037; RRID: AB_2534013), Alexa Fluor Anti-Chicken 488 (1:300, Fisher scientific, A11039), or Alexa Fluor Anti-Mouse 647 (1:300, Life Technologies, A31571; RRID: AB_162542), Alexa Fluor Anti-Rabbit 488 (1:300, Life Technologies, A21206; RRID: AB_2535792). Embryos were stained with DAPI (1 μg/mL) to label nuclei after 3 times washes with wash solution. Embryos were mounted by 2% agarose after washing with PBS. Refer to Key Resource Table.

Imaging

Fixed or live dechorinated embryos are embedded in low-melting 1.5% agarose (Key Resource Table) with the KV positioned at the bottom of a #1.5 glass bottom MatTek plate (Key Resource Table) and imaged using a spinning disk confocal microscope or laser scanning confocal microscope. Zebrafish embryos were imaged using Leica DMi8 (Leica, Bannockburn, IL) equipped with a X-light V2 Confocal unit spinning disk equipped with a Visitron VisiFRAP-DC photokinetics attached to 405 and 355nm

lasers, a Leica SP8 (Leica, Bannockburn, IL) laser scanner confocal microscope (LSCM) and/or a Zeiss LSCM 980 (Carl Zeiss, Germany) with an Airyscan 2 detector. The Leica DMi8 is equipped with a Lumencore SPECTRA X (Lumencore, Beaverton, OR), Photometrics Prime-95B sCMOS Camera, and 89 North-LDi laser launch. VisiView software was used to acquire images. Optics used with this unit are HC PL APO x40/1.10W CORR CS2 0.65 water immersion objective, HC PL APO x40/0.95 NA CORR dry and HCX PL APO x63/1.40-0.06 NA oil objective. The SP8 laser scanning confocal microscope is equipped with HC PL APO 20x/0.75 IMM CORR CS2 objective, HC PL APO 40x/1.10 W CORR CS2 0.65 water objective and HC PL APO x63/1.3 Glyc CORR CS2 glycerol objective. LAS-X software was used to acquire images. The Zeiss LSM 980 is equipped with a T-PMT, GaASP detector, MA-PMT, Airyscan 2 multiplex with 4Y and 8Y. Optics used with this unit are PL APO x63/1.4 NA oil DIC. Zeiss Zen 3.2 was used to acquire the images. A Leica M165 FC stereomicroscope equipped with DFC 9000 GT sCMOS camera was used for staging and phenotypic analysis of zebrafish embryos.

Photoconversion

Tg(sox17:GFP) embryos were injected with 75ng of Dendra-H2B mRNA (see methods in [48]). The embryos were incubated at 30°C until 8 hpf, dechorinated and embeded in 1.5% agarose. To photoconvert H2B-Dendra, 405 nm laser beam was applied to a Region of Interest (ROI) placed over a mitotic plane. The 405 nm laser was used at 8 mW power with 2 FRAP cycles at 50 ms/pixel dwell time. Time-lapse videos were captured using 470 nm and 555 nm lasers to capture green and red emission from non-photoconverted and photoconverted respectively. Z-stacks were acquired at z-stack with a 2 µm step size every 2 minutes until 12 hpf.

Laser Ablation

Tg(sox17:GFP-CAAX; h2afx:h2afv-mCherry) or Tg(sox17:EMTB-3XGFP) decorinated live embryos were imaged on a spinning disk with VisiView kinetics unit

starting at 6 hpf. Time-lapse videos capturing GFP-CAAX and h2afv-mCherry used 470 nm and 555 nm lasers respectively across a z-stack with a 2 µm step size every 2 minutes until 12 hpf. KV mitotic events (all, condition 1-3) were ablated using a 355 nm pulsed laser operating at 65% power. The laser was applied within a ROI over mitotic cell for 2 cycles of 50 ms/pixel. Non-mitotic ablation control involved ablating a region containing 3-8 interphase cells of the KV. Ablated embryos were fixed at 1hpf and stained for cilia (acetylated tubulin).

Image and data analysis

Images were processed using FIJI/ImageJ. Graphs and statistical analysis were produced using Prism 9 software. Additional analysis of KV cells were performed using Bitplane IMARIS software. Videos were created using FIJI/ImageJ or IMARIS. All time-lapse video projections are registered using FIJI. For percentage of ciliated KV cells, the number of cells with cilia was counted and represented as a percentage over the total number of cells in the cyst forming tissue.

Mitotic index and Anterior vs Posterior mitotic event calculation. For mitotic index, the number of mitotic cells (PH3 positive) in the KV was divided by the total number of KV cells (DAPI and Sox17:GFP-CAAX positive), resulting in a percentage of mitotic cells out of the entire population. To calculate fraction of mitotic events in the anterior versus posterior regions, anterior and posterior KV mitotic cell number was divided by the total number of mitotic cells in the KV.

KV Aspect Ratio. KV aspect ratio was calculated from a video projection of Sox17:EMTB-3xGFP embryos from 7 to 12 hpf. Images were acquired at maximum 2 to 3 minute intervals. For each captured frame, the aspect ratio was calculated using FIJI/ImageJ. Longest axis over shortest axis was determined giving the aspect ratio over time. Data was presented by averaging aspect ratios across 10 bins for the

duration of KV development.

Rate in which a spindle rotates. The metaphase derived spindle angle relative to the KV's longest axis was measured over time. To do this, a line was positioned along the longest KV axis in relation to a second line that passes through the two spindle poles and the longest axis of a KV mitotic spindle. The ImageJ/FIJI angle tool calculated the angle at which the two lines intersect providing a spindle angle (∠Spindle). This spindle angle was calculated from metaphase to anaphase completion. The rate in which a spindle rotates was measured by taking the difference of identified spindle angle across time point 1 ($\angle Spindle_{T1}$) and time point 2 ($\angle Spindle_{T2}$) and dividing the difference by time interval (T_1-T_2).

$$Spindle\ Rotation\ Rate = \left|\frac{\angle \mathrm{Spindle}_{\mathrm{T1}} - \angle \mathrm{Spindle}_{\mathrm{T2}}}{\Delta \mathrm{T}_1 - \mathrm{T}_2}\right|$$

Data was presented by averaging spindle rotation rates from each mitotic event across 20 min bins for the duration of KV development between 7 to 12 hpf.

Anterior vs. Posterior Microtubule Intensity.

The mean intensity microtubule ratio between the anterior versus posterior KV was measured using FIJI/ImageJ software in the Sox17: EMTB-3XGFP transgenic line. A square ROI was place over a max-projected KV on the anterior half of the KV and then the posterior half and the mean fluorescence intensities within defined ROIs were obtained. The ratio of anterior to posterior intensity was calculated.

Lumen area.

A region was drawn around the lumen perimeter and area calculated using the measure function. Where applicable, values were normalized to the control mean by dividing each lumen area by the mean value of the control lumens.

Actin intensity measurement at nascent cytokinetic bridge.

KV cells of interest were masked across Z slices at five different time points using Imaris Software. A circular ROI was placed at a newly formed cytokinetic bridge, labeled with EMTB-3xGFP, to quantify actin (lifeact-mRuby) from max-projected datasets over time using the ROI manager in FIJI/ImageJ. Data normalization was performed by dividing the fluorescence intensity at each time point by the mean fluorescence intensity at the final time point for all measured bridges.

Anterior vs. Posterior Microtubule and Actin Intensity.

The mean intensity ratio between the anterior and posterior portions of the KV was quantified using either video projections of Sox17:EMTB-3xGFP embryos for MTs or fixed and stained embryos for actin. The KV, sum-projected from rosette to lumen, was bisected into equal halves, with two ROIs placed on the anterior and posterior portions to measure mean fluorescence intensities. Background fluorescence from adjacent regions was measured and subtracted. The ratio of anterior to posterior intensity was subsequently calculated. For MTs, this measurement and calculation process was repeated at five consecutive time points from a live-video acquisition during rosette-to-lumen formation using the same embryos, and the average ratios were reported. Each point represents an embryo. For actin, this was done at a single fixed rosette stage.

Statistical Analysis

PRISM9 software was used for all graph preparations that include all individual data points across embryos and clutches denoted by color and size of points respectively and as noted in legends. These plots were presented as violin, floating bar, and a modified scatter plot that is termed “super-plot” [49] to denote individual embryos across clutches. Unpaired two-tailed t-tests and one way ANOVA were performed using PRISM9 software. **** denotes a p-value<0.0001, *** p-value<0.001, **p-value<0.01, *p-value<0.05, n.s. not significant. For further information on detailed statistical

analysis see Table S1.

RESOURCE TABLE

Reagent or resource	Source	Identifier
Antibodies		
Acetylated Tubulin	Sigma Aldrich	T6793: RRID: AB_477585
Anti-GFP (Chicken)	GeneTex	GTX13970: AB_371416
Anti-GFP (Rabbit)	Molecular Probes	A-11122: AB_221569
Anti-PH3 (Rabbit)	Cell Signaling Technology	9701S
Anti-BrdU (Mouse)	Sigma-Aldrich	11170376001: BMC9318
Alexa Fluor Anti-Rabbit 488	Life Technologies	A21206; RRID: AB_2535792
Alexa Fluor Anti-Rabbit 568	Life Technologies	A10042; RRID: AB_2534017
Alexa Fluor Anti-Chicken 488	Fisher scientific	A11039
Alexa Fluor Anti-Mouse 568	Life Technologies	A10037; RRID: AB_2534013
Alexa Fluor Anti-Mouse 647	Life Technologies	A31571; RRID: AB_162542
Alexa Fluor® 647 Phalloidin	Cell Signaling Technology	8940S
Chemicals		
DAPI	Sigma Aldrich	D9542-10mg
Agarose	Thermo Fisher	16520100
BSA	Fisher Scientific	BP1600-100
BIO BASIC Maxi Prep Kit	BIO BASIC	9K-0060023

Dimethylsulphoxide	Fisher Scientific	BP231-100
Paraformaldehyde	Fisher Scientific	O4042-500
Phosphate Buffered Saline	Fisher Scientific	10010023
Triton X-100	Fisher Scientific	BP151500
Tween 20	Thermo Fisher	BP337500
Sodium Chloride	Fisher Scientific	BP358
NEBuilder HiFi DNA assembly Cloning Kit	New England BioLabs	E5520S
mMESSAGE mMACHINETMSP6	Invitrogen	AM1340
5-Bromo-2'-deoxyuridine, ≥99% (HPLC)	Sigma-Aldrich	Product Number : B5002 CAS-No. : 59-14-3
XAV939	Sigma-Aldrich	Product Number : X3004 CAS-No. : 284028-89-3
Infigratinib	MedChem Express	Catalog No. : HY-13311 CAS No. : 872511-34-7
Cyclopamine	Sigma-Aldrich	Product Number : PHL82510 CAS-No. : 4449-51-8
Experimental models and strains		
Zebrafish	Zebrafish International Resource Center	AB-Wildtype
Zebrafish	Heidi Hehnly's Lab	Sox17:GFP-CAAX; h2afx:h2afv-mCherry

Zebrafish	Jeffrey Amack Lab	Tg (sox17:GFP-CAAX)sny101
Zebrafish	Li-En Jao Lab	PCNT (-/-)
Zebrafish	Zebrafish International Resource Center	Tg(sox17:GFP)
Zebrafish	Heidi Hehnly's lab	Tg(sox17:EMTB-GFP)
Zebrafish	Heidi Hehnly's lab	sox17:GFP-CAAX;PCNT(-/-)
mRNA		
H2B-Dendra	Heidi Hehnly's lab	Plasmid: pCS2-H2B-Dendra
Lifeact-mRuby	Heidi Hehnly's lab	Plasmid: pCS2-Lifeact-mRuby
mKate-MKLP1	Heidi Hehnly's lab	Plasmid: pCS2-mKate-MKLP1
Software and algorithms		
ImageJ/FIJI	NIH and Laboratory for Optical and Computational Instrumentation	https://imagej.net/Fiji
IMARIS, Bitplane	Oxford Instruments	https://imaris.oxinst.com/
PRISM9	GraphPad	https://www.graphpad.com/scientific-software/prism/
LAS-X Software	Leica Microsystems	https://www.leica-microsystems.com/products/microscope-software/p/leica-las-x-ls/
VisiView	Visitron	https://www.visitron.de/products/visiview-software.html

References Cited

1. Grimes, D. T. & Burdine, R. D. Left–Right Patterning: Breaking Symmetry to Asymmetric Morphogenesis. *Trends in Genetics* **33**, 616–628 (2017).
2. Okabe, N., Xu, B. & Burdine, R. D. Fluid dynamics in zebrafish Kupffer's vesicle. *Dev Dyn* **237**, 3602–3612 (2008).
3. Dasgupta, A. & Amack, J. D. Cilia in vertebrate left-right patterning. *Philos Trans R Soc Lond B Biol Sci* **371**, (2016).
4. Forrest, K., Barricella, A. C., Pohar, S. A., Hinman, A. M. & Amack, J. D. Understanding laterality disorders and the left-right organizer: Insights from zebrafish. *Front Cell Dev Biol* **10**, (2022).
5. McGrath, J., Somlo, S., Makova, S., Tian, X. & Brueckner, M. Two populations of node monocilia initiate left-right asymmetry in the mouse. *Cell* **114**, 61–73 (2003).
6. Layton, W. M. Random determination of a developmental process: reversal of normal visceral asymmetry in the mouse. *J Hered* **67**, 336–338 (1976).
7. Lee, J. D. & Anderson, K. V. Morphogenesis of the node and notochord: the cellular basis for the establishment and maintenance of left-right asymmetry in the mouse. *Dev Dyn* **237**, 3464–3476 (2008).
8. Gredler, M. L. & Zallen, J. A. Multicellular rosettes link mesenchymal-epithelial transition to radial intercalation in the mouse axial mesoderm. *Dev Cell* **58**, 933-950.e5 (2023).
9. Li, D., Mangan, A., Cicchini, L., Margolis, B. & Prekeris, R. FIP5 phosphorylation during mitosis regulates apical trafficking and lumenogenesis. *EMBO Rep* **15**, 428–437 (2014).
10. Mangan, A. J. *et al.* Cingulin and actin mediate midbody-dependent apical lumen formation during polarization of epithelial cells. *Nat Commun* **7**, 12426 (2016).
11. Blasky, A. J., Mangan, A. & Prekeris, R. Polarized protein transport and lumen formation during epithelial tissue morphogenesis. *Annu Rev Cell Dev Biol* **31**, 575–591 (2015).
12. Klinkert, K., Rocancourt, M., Houdusse, A. & Echard, A. Rab35 GTPase couples cell division with initiation of epithelial apico-basal polarity and lumen opening. *Nat Commun* **7**, (2016).
13. Boehlke, C. *et al.* Kif3a guides microtubular dynamics, migration and lumen formation of MDCK cells. *PLoS One* **8**, (2013).
14. Mahjoub, M. R. & Stearns, T. Supernumerary Centrosomes Nucleate Extra Cilia and Compromise Primary Cilium Signaling. *Current Biology* **22**, 1628–1634 (2012).
15. Aljiboury, A. A. *et al.* Rab8, Rab11, and Rab35 coordinate lumen and cilia formation during zebrafish left-right organizer development. *PLoS Genet* **19**, e1010765 (2023).
16. Tavares, B. *et al.* Notch/Her12 signalling modulates, motile/immotile cilia ratio

downstream of Foxj1a in zebrafish left-right organizer. *Elife* **6**, (2017).
17. Neugebauer, J. M., Amack, J. D., Peterson, A. G., Bisgrove, B. W. & Yost, H. J. FGF signalling during embryo development regulates cilia length in diverse epithelia. *Nature* **458**, 651–654 (2009).
18. Meyers, E. N. & Martin, G. R. Differences in left-right axis pathways in mouse and chick: functions of FGF8 and SHH. *Science* **285**, 403–406 (1999).
19. Caron, A., Xu, X. & Lin, X. Wnt/β-catenin signaling directly regulates Foxj1 expression and ciliogenesis in zebrafish Kupffer's vesicle. *Development* **139**, 514–524 (2012).
20. Sepulveda, G. *et al.* Co-translational protein targeting facilitates centrosomal recruitment of PCNT during centrosome maturation. *Co-translational protein targeting facilitates centrosomal recruitment of PCNT during centrosome maturation in vertebrates* **7**, 241083 (2018).
21. Mikule, K. *et al.* Loss of centrosome integrity induces p38—p53—p21-dependent G1—S arrest. *Nature Cell Biology 2006 9:2* **9**, 160–170 (2006).
22. Purohit, A., Tynan, S. H., Valle, R. & Doxsey, S. J. Direct Interaction of Pericentrin with Cytoplasmic Dynein Light Intermediate Chain Contributes to Mitotic Spindle Organization. *J Cell Biol* **147**, 481 (1999).
23. Chen, C.-T. T. *et al.* A Unique Set of Centrosome Proteins Requires Pericentrin for Spindle-Pole Localization and Spindle Orientation. *Current Biology* **24**, 2327–2334 (2014).
24. Delaval, B. & Doxsey, S. J. Pericentrin in cellular function and disease. *J Cell Biol* **188**, 181–190 (2010).
25. Zimmerman, W. C., Sillibourne, J., Rosa, J. & Doxsey, S. J. Mitosis-specific anchoring of γ tubulin complexes by pericentrin controls spindle organization and mitotic entry. *Mol Biol Cell* **15**, 3642–3657 (2004).
26. Bergstralh, D. T., Dawney, N. S. & St Johnston, D. Spindle orientation: a question of complex positioning. *Development* **144**, 1137–1145 (2017).
27. Vertii, A., Kaufman, P. D., Hehnly, H. & Doxsey, S. New dimensions of asymmetric division in vertebrates. *Cytoskeleton* vol. 75 87–102 Preprint at https://doi.org/10.1002/cm.21434 (2018).
28. Rathbun, L. I. *et al.* PLK1- and PLK4-Mediated Asymmetric Mitotic Centrosome Size and Positioning in the Early Zebrafish Embryo. *Current Biology* **30**, 4519-4527.e3 (2020).
29. Gudipaty, S. A. & Rosenblatt, J. Epithelial Cell Extrusion: pathways and pathologies. *Semin Cell Dev Biol* **67**, 132 (2017).
30. Essner, J. J., Amack, J. D., Nyholm, M. K., Harris, E. B. & Yost, H. J. Kupffer's vesicle is a ciliated organ of asymmetry in the zebrafish embryo that initiates left-right development of the brain, heart and gut. *Development* **132**, 1247–1260 (2005).
31. Guizetti, J. *et al.* Cortical constriction during abscission involves helices of ESCRT-III-dependent filaments. *Science* **331**, 1616–1620 (2011).
32. Addi, C., Bai, J. & Echard, A. Actin, microtubule, septin and ESCRT filament

remodeling during late steps of cytokinesis. *Curr Opin Cell Biol* **50**, 27–34 (2018).
33. Rathbun, L. I. *et al.* Cytokinetic bridge triggers de novo lumen formation in vivo. *Nat Commun* **11**, 1–12 (2020).
34. Harding, M. J., McGraw, H. F. & Nechiporuk, A. The roles and regulation of multicellular rosette structures during morphogenesis. *Development* **141**, 2549 (2014).
35. Takeshita, N., Manck, R., Grün, N., de Vega, S. H. & Fischer, R. Interdependence of the actin and the microtubule cytoskeleton during fungal growth. *Curr Opin Microbiol* **20**, 34–41 (2014).
36. Martin, S. G., McDonald, W. H., Yates, J. R. & Chang, F. Tea4p links microtubule plus ends with the formin for3p in the establishment of cell polarity. *Dev Cell* **8**, 479–491 (2005).
37. Wu, S. Z. & Bezanilla, M. Actin and microtubule cross talk mediates persistent polarized growth. *J Cell Biol* **217**, 3531 (2018).
38. Sanchez, A. D. & Feldman, J. L. Microtubule-organizing centers: from the centrosome to non-centrosomal sites. *Curr Opin Cell Biol* **44**, 93–101 (2017).
39. Cheng, H. *et al.* Actin filaments form a size-dependent diffusion barrier around centrosomes. *EMBO Rep* **24**, (2023).
40. Dunkley, S. & Mogessie, B. Actin limits egg aneuploidies associated with female reproductive aging. *Sci Adv* **9**, (2023).
41. Farina, F. *et al.* The centrosome is an actin-organizing centre. *Nat Cell Biol* **18**, 65–75 (2016).
42. Magescas, J., Eskinazi, S., Tran, M. V. & Feldman, J. L. Centriole-less pericentriolar material serves as a microtubule organizing center at the base of C. elegans sensory cilia. *Curr Biol* **31**, 2410-2417.e6 (2021).
43. Zenker, J. *et al.* A microtubule-organizing center directing intracellular transport in the early mouse embryo. *Science* **357**, 925–928 (2017).
44. Krishnan, N. *et al.* Rab11 endosomes and Pericentrin coordinate centrosome movement during pre-abscission in vivo. *Life Sci Alliance* **5**, 1–15 (2022).
45. Hannaford, M. R. & Rusan, N. M. Positioning centrioles and centrosomes. *J Cell Biol* **223**, (2024).
46. Hannaford, M. R. *et al.* Pericentrin interacts with Kinesin-1 to drive centriole motility. *J Cell Biol* **221**, (2022).
47. Kimmel, C. B., Ballard, W. W., Kimmel, S. R., Ullmann, B. & Schilling, T. F. Stages of embryonic development of the zebrafish. *Developmental dynamics : an official public* **203**, 253–310 (1995).
48. Aljiboury, A. A., Mujcic, A., Cammerino, T., Rathbun, L. I. & Hehnly, H. Imaging the early zebrafish embryo centrosomes following injection of small-molecule inhibitors to understand spindle formation. *STAR Protoc* **2**, 100293 (2021).
49. Lord, S. J., Velle, K. B., Dyche Mullins, R. & Fritz-Laylin, L. K. SuperPlots: Communicating reproducibility and variability in cell biology. *Journal of Cell Biology* **219**, (2020).

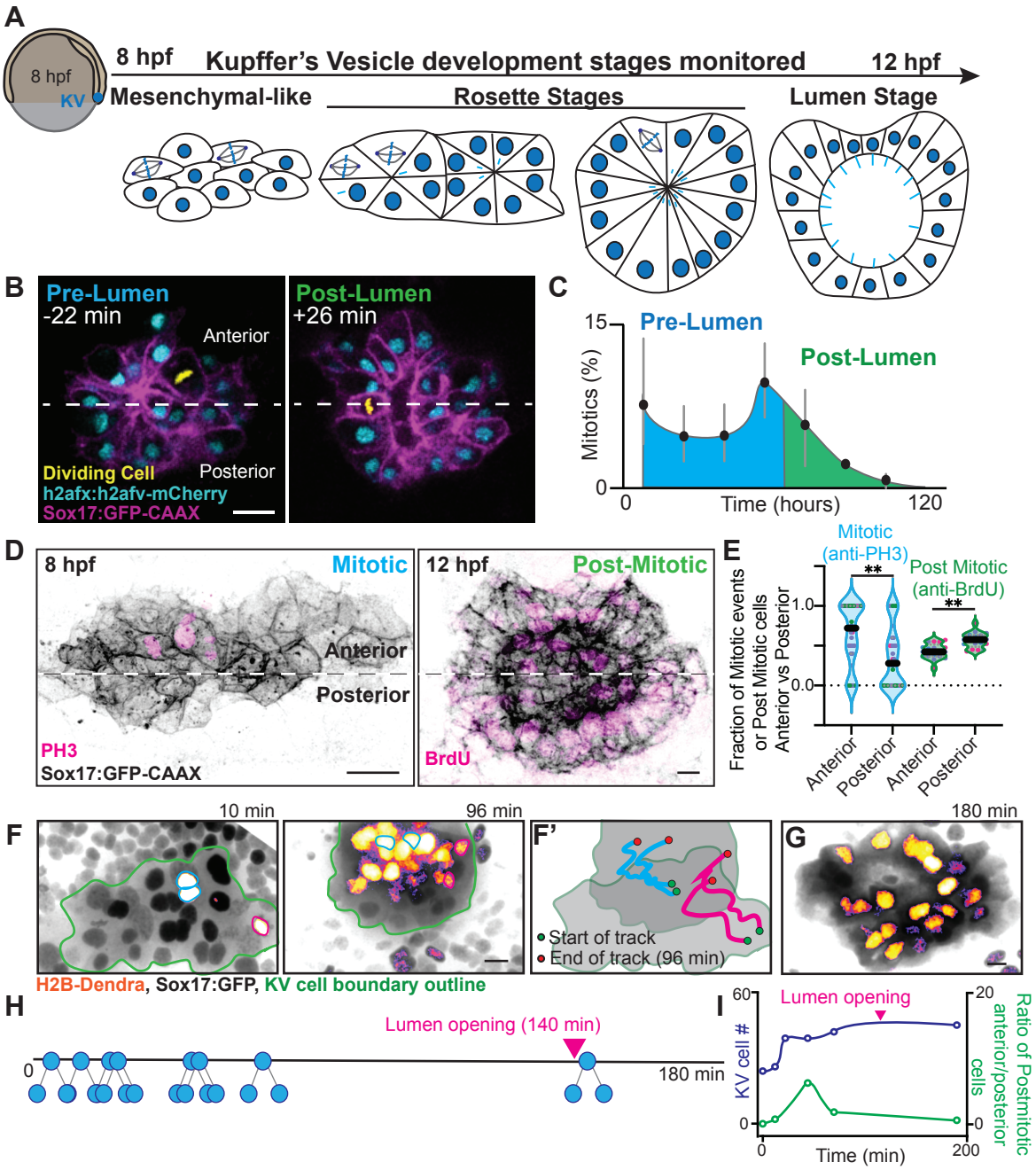

Fig 1. Identification of an anteriorly positioned and pre-lumen enriched KV mitotic events and their post-mitotic distribution map.

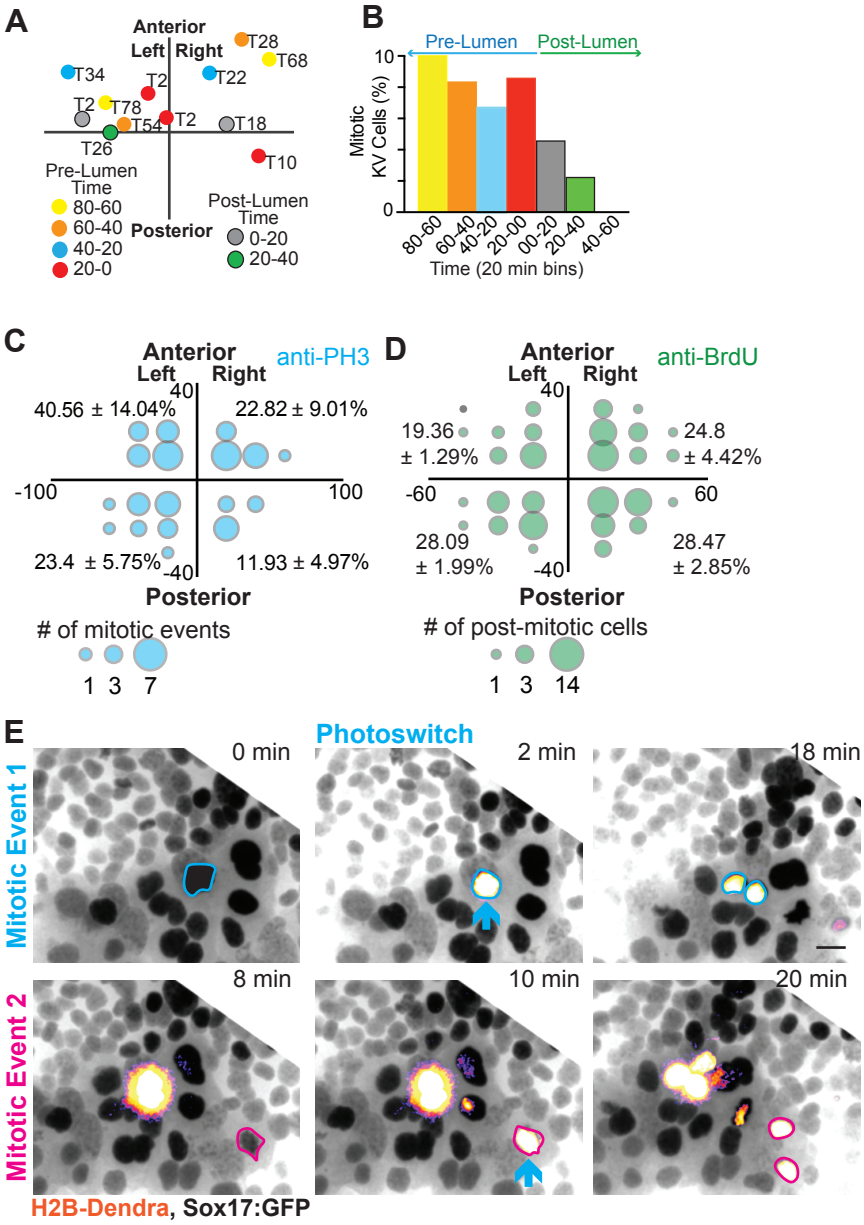

Fig S1. Identification of an anteriorly positioned and pre-lumen enriched KV mitotic events and their post-mitotic distribution map.

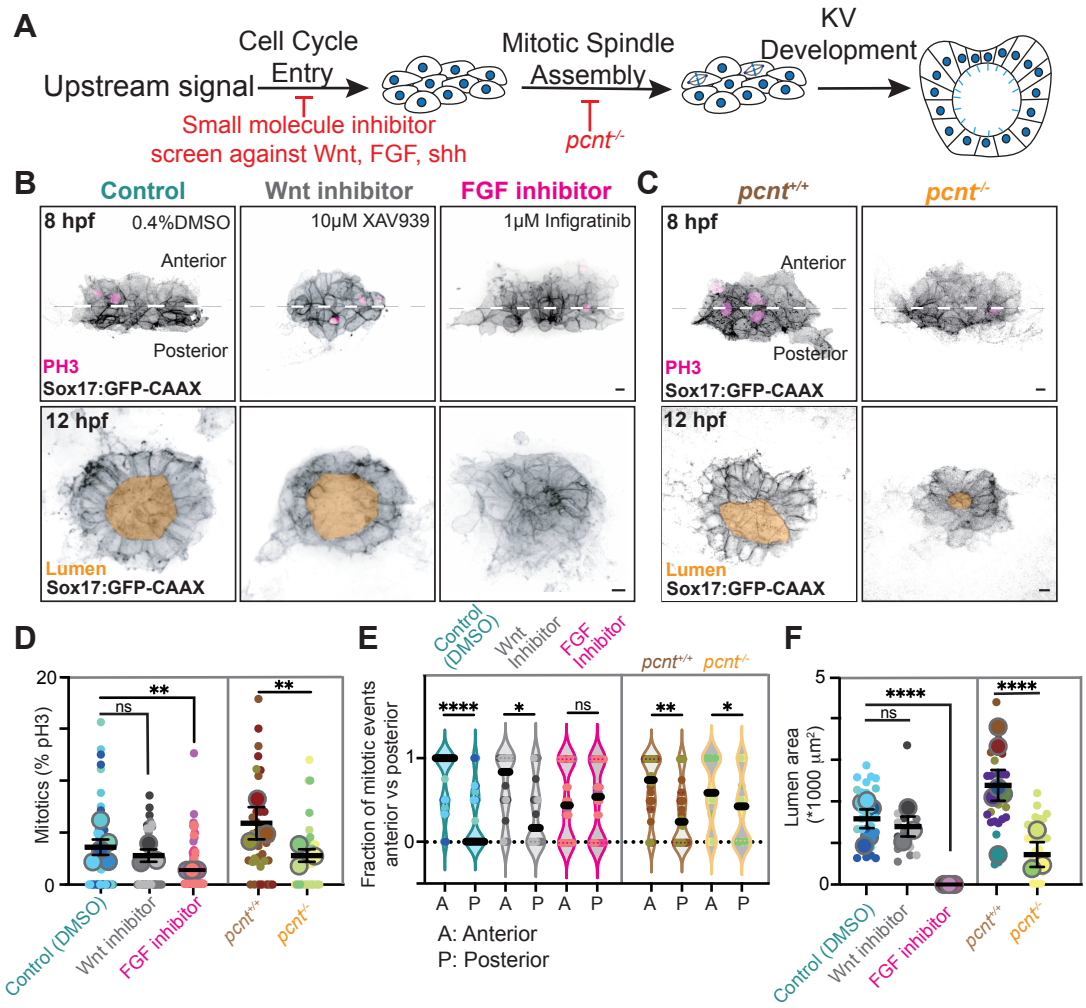

Fig 2. An anterior/posterior FGF signaling gradient is required for anterior zones of mitotic activity.

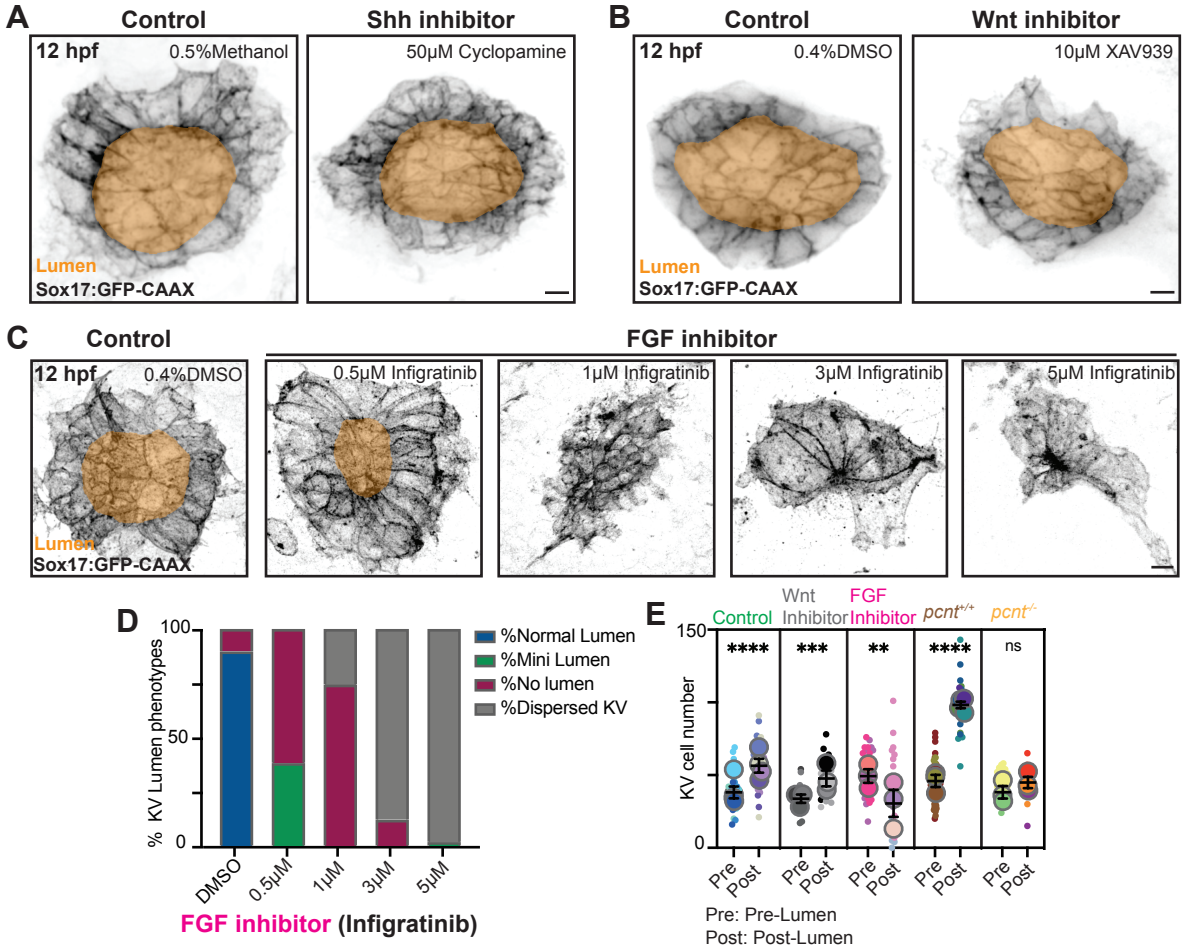

Fig S2. An anterior/posterior FGF signaling gradient is required for anterior zones of mitotic activity.

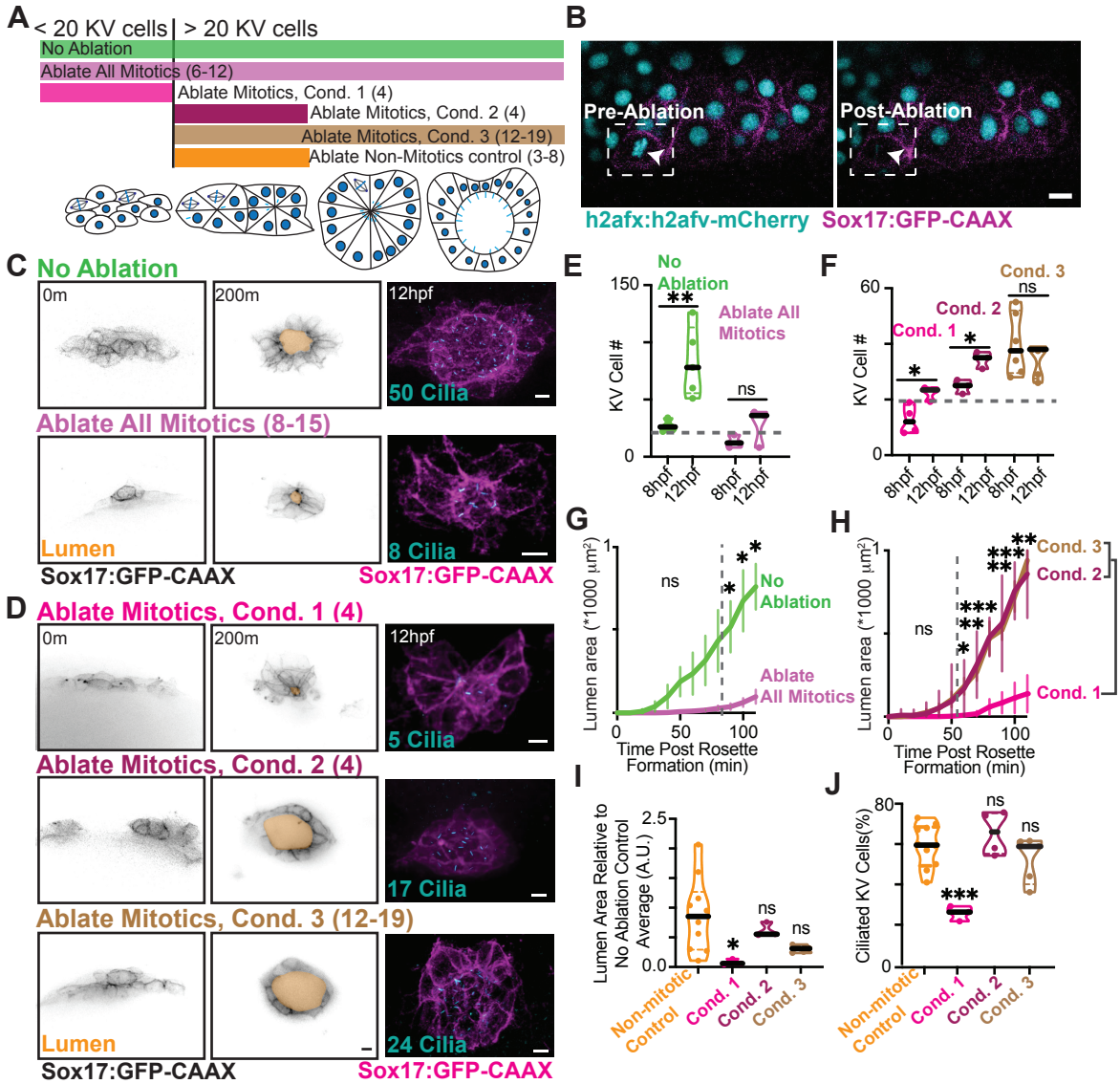

Fig 3. Early KV mitotic events hold greater significance to KV development compared to later KV mitotic events.

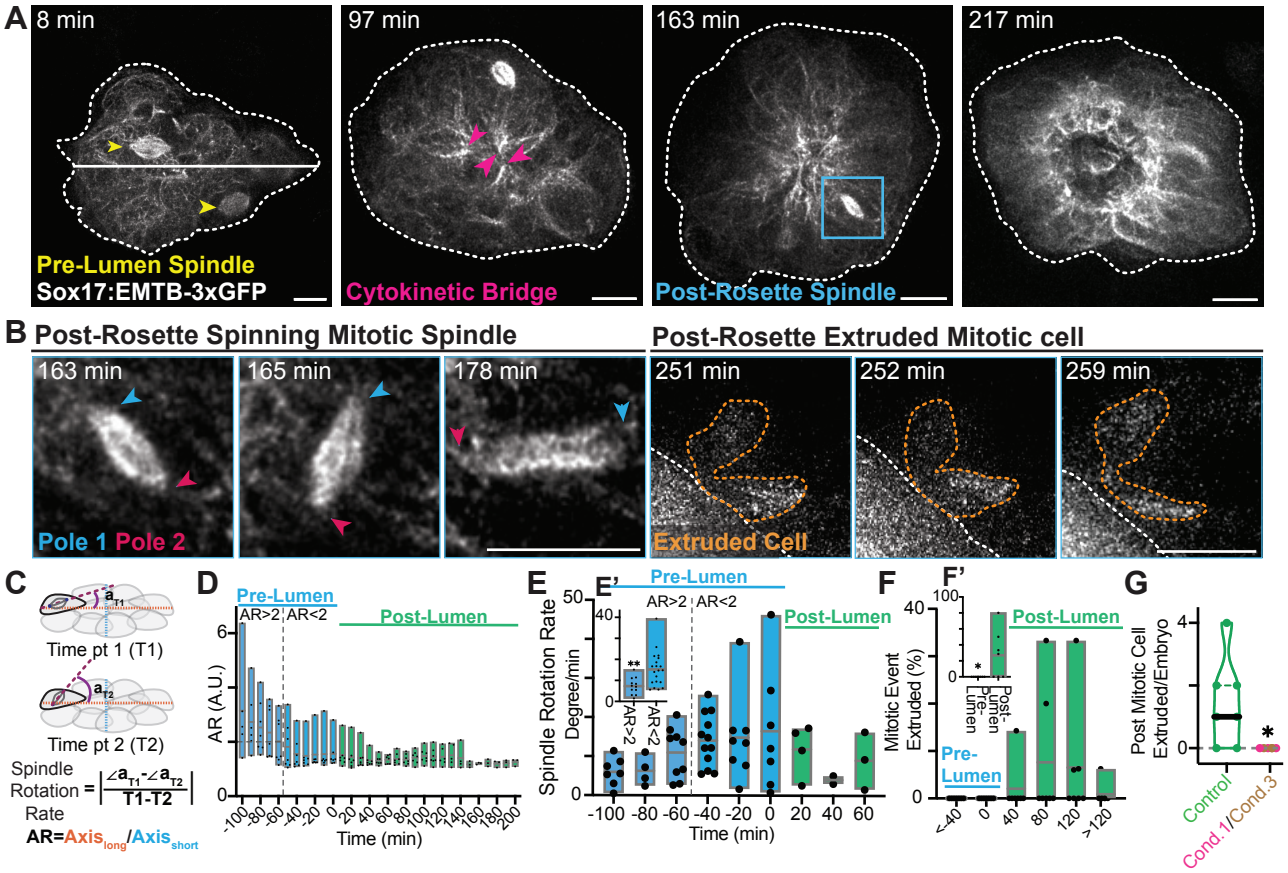

Fig 4. KV spindles stably align along KVs longest axis until the KV starts rounding, then spindles spin and are extruded.

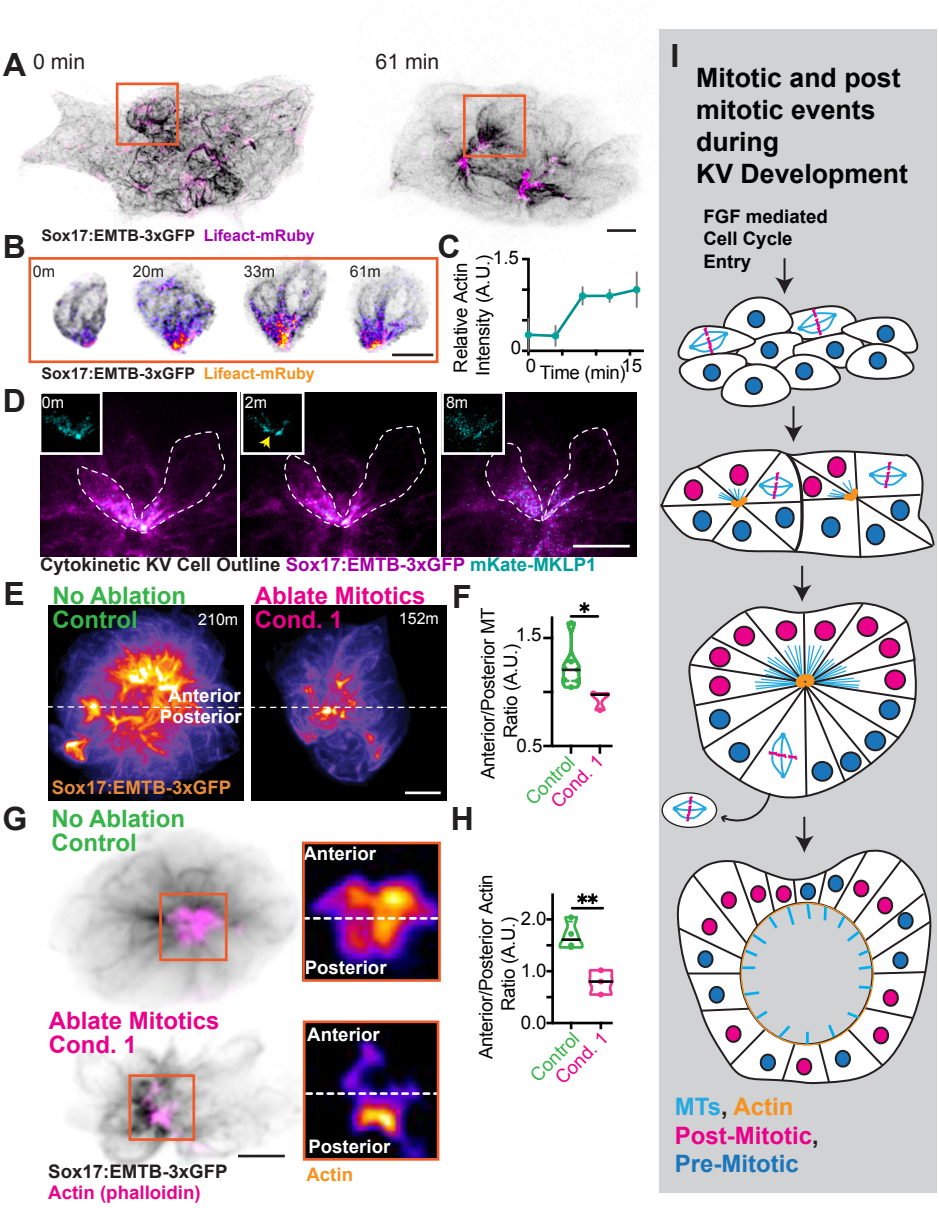

Fig 5. Anterior division events lead to anterior focused cytokinetic bridge remnant MT bundles at the rosette which precede actin recruitment.

Table S1. Detailed statistical analysis of results reported in this study.

Figure	Category	n embryo	n Clutch	Statistical Test	Parameters	Result	p-value
1C	%Mitotic KV cells	3	3	N/A	N/A	N/A	N/A
1E	pH3 positive cell Anterior	36	4	Unpaired t-test	t=5.409, df=6	N/A	N/A
	pH3 positive cell Posterior					**	0.0016
	BrdU positive cell Anterior	17	3	Unpaired t-test	t=4.627, df=4	N/A	N/A
	BrdU positive cell Posterior					**	0.0098
1I	Ratio of Postmitotic anterior/posterior cell	1	1	N/A	N/A	N/A	N/A
S1A	%Mitotic KV cells	1	1	N/A	N/A	N/A	N/A
S1B	Position of the PH3 positive cell	1	1	N/A	N/A	N/A	N/A
S1C	pH3 positive cell	26	3	N/A	N/A	N/A	N/A
S1D	BrdU positive cell	3	3	N/A	N/A	N/A	N/A
2D	DMSO	53	5	One Way ANOVA (multiple compariso n)	F (2,1.51) =5.621	N/A	N/A
	XAV939	33	3			n.s.	0.4369
	Infigratinib	68	3			**	0.0022
	pcnt (+/+)	46	3	Unpaired t-test	t=2.638, df=89	N/A	N/A
	pcnt (-/-)	45	3			**	0.0098
2E	DMSO	34	5	Unpaired t-test	t=4.447, df=64	****	<0.0001
	XAV939	20	3	Unpaired t-test	t=2.262, df=38	*	0.0295
	Infigratinib	34	3	Unpaired t-test	t=0.03508, df=66	n.s.	0.9721
	pcnt (+/+)	31	3	Unpaired t-test	t=3.440, df=60	**	0.0011
	pcnt (-/-)	30	3	Unpaired t-test	t=2.199, df=58	*	0.0319

2F	DMSO	29	5	One Way ANOVA (multiple comparison)	F (2,71) = 76.33	N/A	N/A
	XAV939	16	3			n.s.	0.2
	Infigratinib	29	3			****	<0.0001
	pcnt (+/+)	16	4	Unpaired t-test	t=6.018, df=57	N/A	N/A
	pcnt (-/-)	29	3			****	<0.0001
S2D	DMSO	39	2	N/A	N/A	N/A	N/A
	0.5μM Infigratinib	34	2	N/A	N/A	N/A	N/A
	1μM Infigratinib	39	2	N/A	N/A	N/A	N/A
	3μM Infigratinib	25	2	N/A	N/A	N/A	N/A
	5μM Infigratinib	57	2	N/A	N/A	N/A	N/A
S2E	DMSO pre-lumen stage	36	5	Unpaired t-test	t=5.693, df=71	N/A	N/A
	DMSO post-lumen stage	37	4			****	<0.0001
	XAV939 pre-lumen stage	22	3	Unpaired t-test	t=3.679, df=36	N/A	N/A
	XAV939 post-lumen stage	16	3			***	0.0008
	Infigratinib pre-lumen stage	32	3	Unpaired t-test	t=3.032, df=59	N/A	N/A
	Infigratinib post-lumen stage	29	3			**	0.0036
	pcnt (+/+) pre-lumen stage	54	3	Unpaired t-test	t=14.55, df=75	N/A	N/A
	pcnt (+/+) post-lumen stage	23	4			****	<0.0001
	pcnt (-/-) pre-lumen stage	35	3	Unpaired t-test	t=1.906, df=56	N/A	N/A
	pcnt (-/-) post-lumen stage	23	3			n.s.	0.0617
3E	No Ablation 8hpf	4	4	Unpaired t-test	t=3.586, df=7	**	0.0089
	No Ablation 12hpf	5	5				
	Ablate All Mitotics 8hpf	3	3	Unpaired t-test	t=1.413, df=4	n.s.	0.2306

	Ablate All Mitotics 12hpf	3	3				
3F	Cond. 1_8hpf	4	4	Unpaired t-test	t=2.782, df=5	*	0.0388
	Cond. 1_12hpf	3	3				
	Cond. 2_8hpf	3	3	Unpaired t-test	t=4.230, df=4	*	0.0134
	Cond. 2_12hpf	3	3				
	Cond. 3_8hpf	6	6	Unpaired t-test	t=1.040, df=9	n.s.	0.3257
	Cond. 3_12hpf	5	5				
3G	Lumen area: No ablation control 20min	3	3	Unpaired t-test	t=1.000, df=4	n.s.	0.3739
	Lumen area: All mitotic ablated 20min	3	3				
	Lumen area: No ablation control 30min	3	3	Unpaired t-test	t=1.231, df=4	n.s.	0.2856
	Lumen area: All mitotic ablated 30min	3	3				
	Lumen area: No ablation control 40min	3	3	Unpaired t-test	t=1.356, df=4	n.s.	0.2466
	Lumen area: All mitotic ablated 40min	3	3				
	Lumen area: No ablation control 50min	3	3	Unpaired t-test	t=2.049, df=4	n.s.	0.1098
	Lumen area: All mitotic ablated 50min	3	3				
	Lumen area: No ablation control 60min	3	3	Unpaired t-test	t=1.777, df=4	n.s.	0.1503
	Lumen area: All mitotic ablated 60min	3	3				

	Lumen area: No ablation control 70min	3	3	Unpaired t-test	t=2.000, df=4	n.s.	0.1161
	Lumen area: All mitotic ablated 70min	3	3				
	Lumen area: No ablation control 80min	3	3	Unpaired t-test	t=2.174, df=4	n.s.	0.0954
	Lumen area: All mitotic ablated 80min	3	3				
	Lumen area: No ablation control 90min	3	3	Unpaired t-test	t=3.096, df=4	*	0.0364
	Lumen area: All mitotic ablated 90min	3	3				
	Lumen area: No ablation control 100min	3	3	Unpaired t-test	t=3.298, df=4	*	0.0300
	Lumen area: All mitotic ablated 100min	3	3				
	Lumen area: No ablation control 110min	3	3	Unpaired t-test	t=4.597, df=4	*	0.0101
	Lumen area: All mitotic ablated 110min	3	3				
3H	Lumen area: Cond. 1_10min	3	3	One Way ANOVA (multiple comparison)	F (2, 6) = 0.5000"	N/A	N/A
	Lumen area: Cond. 2_10min	3	3			n.s.	0.6180
	Lumen area: Cond. 3_10min	4	4			n.s.	0.6180
	Lumen area: Cond. 1_20min	3	3	One Way ANOVA (multiple comparison)	F (2, 6) = 0.5000"	N/A	N/A
	Lumen area: Cond. 2_20min	3	3			n.s.	0.6180
	Lumen area: Cond. 3_20min	4	4			n.s.	0.6180

	Lumen area: Cond. 1_30min	3	3	One Way ANOVA (multiple comparison)	F (2, 6) = 0.7719"	N/A	N/A
	Lumen area: Cond. 2_30min	3	3			n.s.	0.4955
	Lumen area: Cond. 3_30min	4	4			n.s.	0.4955
	Lumen area: Cond. 1_40min	3	3	One Way ANOVA (multiple comparison)	F (2, 6) = 2.493"	N/A	N/A
	Lumen area: Cond. 2_40min	3	3			n.s.	0.1697
	Lumen area: Cond. 3_40min	4	4			n.s.	0.1697
	Lumen area: Cond. 1_50min	3	3	One Way ANOVA (multiple comparison)	F (2, 6) = 1.520"	N/A	N/A
	Lumen area: Cond. 2_50min	3	3			n.s.	0.2945
	Lumen area: Cond. 3_50min	4	4			n.s.	0.2945
	Lumen area: Cond. 1_60min	3	3	One Way ANOVA (multiple comparison)	F (2, 6) = 8.375"	N/A	N/A
	Lumen area: Cond. 2_60min	3	3			*	0.0215
	Lumen area: Cond. 3_60min	4	4			*	0.0215
	Lumen area: Cond. 1_70min	3	3	One Way ANOVA (multiple comparison)	F (2, 6) = 19.10"	N/A	N/A
	Lumen area: Cond. 2_70min	3	3			**	0.0031
	Lumen area: Cond. 3_70min	4	4			**	0.0031
	Lumen area: Cond. 1_80min	3	3	One Way ANOVA (multiple comparison)	F (2, 6) = 48.23"	N/A	N/A
	Lumen area: Cond. 2_80min	3	3			***	0.0003
	Lumen area: Cond. 3_80min	4	4			***	0.0003
	Lumen area: Cond. 1_90min	3	3	One Way ANOVA (multiple comparison)	F (2, 6) = 17.48"	N/A	N/A
	Lumen area: Cond. 2_90min	3	3			**	0.0039
	Lumen area: Cond. 3_90min	4	4			**	0.0039

	Lumen area: Cond. 1_100min	3	3	One Way ANOVA (multiple comparison)	F (2, 6) = 35.51"	N/A	N/A
	Lumen area: Cond. 2_100min	3	3			***	0.0006
	Lumen area: Cond. 3_100min	4	4			***	0.0006
	Lumen area: Cond. 1_110min	3	3	One Way ANOVA (multiple comparison)	F (2, 6) = 25.79"	N/A	N/A
	Lumen area: Cond. 2_110min	3	3			**	0.0016
	Lumen area: Cond. 3_110min	4	4			**	0.0016
3I	Non-mitotic Control	10	6	One Way ANOVA (multiple comparison)	F (3, 17) = 3.302	N/A	N/A
	Ablate Mitotic Cond. 1	3	3			*	0.0493
	Ablate Mitotic Cond.2	4	4			n.s.	0.7471
	Ablate Mitotic Cond. 3	5	5			n.s.	0.0893
3J	Non-mitotic Control	10	6	One Way ANOVA (multiple comparison)	F (3, 18) = 9.935	N/A	N/A
	Ablate Mitotic Cond. 1	3	3			***	0.0003
	Ablate Mitotic Cond. 2	4	4			n.s.	0.6507
	Ablate Mitotic Cond. 3	5	5			n.s.	0.5365
4 D	Aspect Ratio of KV	7	6	N/A	N/A	N/A	N/A
4 E'	A.R.>2	12 cells (7 embryos)	6	Unpaired t-test	t=3.114, df=30	N/A	0.0040
	A.R.<2	20 cells (7 embryos)	6			**	0.6507
4 F'	Pre-Lumen	7	6	Unpaired t-test	t=2.381, df=12	N/A	0.0347
	Post Lumen	7	6			*	
4 G	No Ablation Control	7	6	Unpaired t-test	t=2.488, df=11	N/A	0.0301
	Ablate Mitotics Cond. 1 and 3	6	6			*	

5 F	No ablation control	7	6	Unpaired t-test	t=2.424, df=8	N/A	0.0416
	Ablate Mitotic Cond. 1	3	3			*	
5H	No ablation control	4	3	Unpaired t-test	t=4.588, df=5	N/A	0.0059
	Ablate Mitotic Cond. 1	3	3			**	